Journal of Catalysis 323 (2015) 19–32

Contents lists available at ScienceDirect

Journal of Catalysis

journal homepage: www.elsevier.com/locate/jcat

The role of oxide location in HMF etherification with ethanol over sulfated ZrO_2 supported on SBA-15

K. Barbera [a], P. Lanzafame [a,*], A. Pistone [a], S. Millesi [b], G. Malandrino [b], A. Gulino [b], S. Perathoner [a], G. Centi [a]

[a] Department of Electronic Engineering, Chemistry and Industrial Engineering and CASPE-INSTM, University of Messina, 98166 Messina, Italy
[b] Department of Chemistry, University of Catania and INSTM UdR of Catania, Viale Andrea Doria 6, 95125 Catania, Italy

ARTICLE INFO

Article history:
Received 28 April 2014
Revised 17 November 2014
Accepted 7 December 2014

Keywords:
HMF etherification
ZrO_2/SBA-15
Sulfated zirconia
Lewis acid sites
Oxide location on SBA-15

ABSTRACT

The etherification of 5-hydroxymethyl-2-furfural (HMF) over ZrO_2 and sulfated ZrO_2-SBA-15 was chosen as a case study to analyze (i) the quantitative relationship between the concentration of Lewis and Brønsted acid sites and the catalytic behavior in the above reaction, which is also of industrial relevance for the production of biodiesel additives, and (ii) how the location of zirconia nanoparticles inside or outside the mesoporous channels of SBA-15 could significantly influence the specific reactivity in this reaction, both before and after sulfation. Depending on the loading of zirconia (about 10 or 35 wt%), the characterization data by different techniques (TEM, XRD, BET, Dr-UV–vis, and XPS) agree in indicating that zirconia is located predominantly outside the mesoporous channels as small zirconia nanoparticles for the lower loading, and predominantly inside the mesoporous channels for the higher loading. The concentration of medium–strong Lewis and Brønsted acid sites were determined by pyridine chemisorption monitored by IR spectroscopy. While the concentration of Brønsted acid sites (formed after sulfation) is linearly dependent on the amount of zirconia in SBA-15, a marked deviation is observed for Lewis acid sites. The same conclusion was derived from analysis of the dependence of the catalytic activity in Lewis- or Brønsted-acid-site-promoted reactions. The analysis of these results indicated that the characteristics of the zirconia nanoparticles deposited outside or inside the mesoporous silica channels differ in terms of acid features and in turn of catalytic reactivity.

1. Introduction

There is increasing interest in the use of oxides supported on mesoporous silica materials as catalysts, particularly SBA-15, which has ordered channels with larger size than those in MCM-41. In the field of biomass conversion, SBA-15 may provide a way to increase the active surface area of the supported oxide, while limiting the number of micropores, which can be detrimental to selectivity in the transformation of bulky molecules. For this reason, various authors have recently studied oxides supported on SBA-15 in this type of reactions. Zirconia was often utilized as an oxide for its acid–base properties [1–4] (tunable by sulfation [5–7]) and for the presence of both Lewis and Brønsted acid sites. There is general interest in the development of solid acid catalysts containing both Brønsted and Lewis acid sites for the conversion in the aqueous phase of molecules of interest for biomass conversion [8–10].

Recent studies have evidenced that in the etherification of 5-hydroxymethylfurfural (HMF) with alcohol over ZrO_2 supported on mesoporous silica, the type and strength of acidity considerably influence the path of transformation and selectivity [11,12].

Several authors have also investigated the esterification of aldehydes, phenols, and acids in bio-oils [13–15]. Kuwahara et al. [16] have investigated the esterification of levulinic acid with ethanol over sulfated Zr-SBA-15 catalysts, observing a correlation between the catalytic activity and the density of acid sites. They also remarked that the dispersion of the acid sites and the associated accessibility of the reactants play an important role in determining the overall activity. Sulfated zirconia on SBA-15 was also investigated for cellobiose hydrolysis [17], and a correlation with Brønsted acidity was indicated, but not quantified. Therefore, there is general interest in studying these catalysts in various types of reactions of interest for biomass conversion, particularly etherification or esterification reactions, where a relation between the acidity and the catalytic activity was observed, but never quantified. A promotional role of SBA-15 as a support (over the unsupported oxide) was observed, but the reasons were not analyzed in detail.

* Corresponding author.
E-mail address: planzafame@unime.it (P. Lanzafame).

http://dx.doi.org/10.1016/j.jcat.2014.12.001
0021-9517/

We may remark that oxides in mesoporous silica may be present in various forms, although their specific catalytic role was not clearly identified. The oxide may be present as nanocrystallites deposited on the external surfaces of crystallites, inside the channels, or forming monolayer-type species (mono- or polynuclear species formed by reaction with surface silanol groups), which may lead to the reconstruction of the inner walls of the mesoporous channels (the so-called corona area [18,19]). Katryniok et al. [20] observed that by grafting zirconia onto SBA-15, a very high dispersion of zirconia within the mesoporous silica (indicated as a nanocomposite) could be obtained, with a linear relationship between the amount of introduced zirconia and the number of acid sites. On the other hand, Schlögl and co-workers [21] observed that upon introduction of molybdenum oxide species into the channels of SBA-15, the limited availability of anchor silanol groups at high loadings forced the MoO_4 groups to form strained configurations, giving enhanced reactivity and reasonably different acid-based properties. A similar mechanism probably occurs for zirconia, suggesting that a nonlinear correlation between the concentration of zirconia species and acidity/reactivity is expected.

Ballem et al. [22] noted that zirconia nanoparticles inside SBA-15 have small dimensions (~4 nm) and are faceted with 110 surfaces termination, suggesting enhanced reactivity and acidity with respect to nanoparticles deposited on the external surface. Wang et al. [23] observed that the acid strength of sulfated ZrO_2/MCM-41 (with monolayer coverage) is lower than that of bulk sulfated zirconia, in contrast with the other indications discussed above and for example with what was found by Gao et al. [24] in the esterification of oleic acid.

There are thus contradictory results on the influence of the location of oxide species in SBA-15 on their properties and reactivity. Intuitively, small oxide nanoparticles deposited on the external surface of a porous support could be preferable, because (i) the interaction with silanol groups is reduced (most are present inside the channels [25,26]) and (ii) the accessibility of bulky molecules is higher. Although in theory the channel diameter in SBA-15 (around 6–9 nm, depending on the preparation) avoids the presence of diffusional problems, the length of channels (typically in the range 300–600 nm) may create issues of full access to active sites in the inner part of the channels [27,28]. Similarly, the deposition of the oxide may not occur in the whole channels, but only at or close to the entrances of the mesopores [29]. Landau et al. [30] remarked how TiO_2 and ZrO_2 can be inserted inside the pores of SBA-15 in different locations depending on the preparation. Janssen et al. [31] observed that small zirconia particles (2–3 nm) inside the mesopores of SBA-15 are not distributed uniformly in all the channels.

The objective of this paper is thus to understand better how the location of zirconia in ZrO_2/SBA-15 catalysts influences the acidity and catalytic activity in reactions of biomass conversion sensitive to acidity characteristics and how the sulfation of these samples would influence these properties. As a reaction highly sensitive to the acid characteristics of the catalysts (type and strength of the acid sites) in terms of different transformation pathways, we have selected 5-hydroxymethyl-2-furfural (HMF) etherification with ethanol. A reason for interest in this reaction, in addition to its being a model reaction to analyze the acid characteristics of the catalyst as discussed below, is that the products obtained are of commercial interest as high-cetane-number biodiesel additives [32,33]. Three main types of products could be detected [12]: 5-(ethoxymethyl)furan-2-carbaldehyde (EMF), 1,1-diethoxyethane (DE), and ethyl 4-oxopentanoate (EOP) (Scheme 1).

The selectivity to EMF and EOP was related to the presence of Lewis and/or Brønsted acidity on the catalyst, while the formation of DE depended on defect sites, which, being less reactive, catalyzed the side reaction of co-reactant ethanol to DE only when strong Lewis and/or Brønsted acid sites were absent.

Luo et al. [11] showed recently that under pressure (70 bar) in HMF etherification with 2-propanol, catalysts with Lewis acidity or weak Brønsted acidity are active in the transfer of hydrogen from the alcohol to HMF to produce 2,5-bis(hydroxymethyl)furan (in their case), with subsequent reactions to form mono- or diethers. However, at lower pressure and using a primary alcohol, this reaction was negligible, thus reducing in part the complexity of the reaction network.

Therefore, HMF etherification with ethanol is a useful model system (besides its applicative interest) to analyze the role of the location of the oxide in ZrO_2/SBA-15-based catalysts on the acid properties and in turn the catalytic reactivity. However, understanding the role of location also requires having good model catalysts with different locations of the oxide, for which analysis may thus provide insight into the above aspects. In preparing ZrO_2/SBA-15 catalysts, we observed (as detailed later) that a different location of ZrO_2 is observed depending on the initial loading, with preferential external or internal deposition of small nanoparticles at 10 and 35 wt%, respectively. The reasons for this effect are still under investigation (probably related to the gradients of concentration realized during the preparation), but these two catalysts, before and after sulfation of zirconia, and in comparison with pure SBA-15 and ZrO_2 (before and after sulfation) samples, were good model systems to understand the effect of oxide location in oxide/mesoporous systems in the acid characteristics and in turn the catalytic behavior.

2. Experimental

2.1. Catalyst preparation

Mesoporous SBA-15 was prepared as a support according to the synthesis procedure in the literature and the detailed procedure described elsewhere [34]. Different ZrO_2 loadings (theoretical 10 and 35 wt%) were dispersed on the SBA-15 support by a urea hydrolysis method using zirconium(IV) oxychloride ($ZrOCl_2{\cdot}8H_2O$) as a zirconia source [35]. The mixture was refluxed at 90 °C for 5 h (pH about 8), and the resulting gel was filtered and washed with distilled water until removal of chloride. After centrifugation, the ZrO_2-SBA-15 gel was dried and calcined at 550 °C for 6 h. The samples are indicated hereafter as $Z_{x\%}$-SBA.

Pure ZrO_2 was prepared by the sol–gel method. A portion of 20 ml of zirconium *n*-propoxide was mixed with 26.6 ml of *n*-propanol and stirred with a magnetic stir bar. Then 2.8 ml of water was added dropwise to carry out the hydrolysis and gelation of zirconium *n*-propoxide. The gel was aged for 1 h at room temperature and then placed in an oil bath at 75 °C to remove alcohol. The solid was then dried at 120 °C for 12 h and calcined at 550 °C for 12 h [36]. This reference material is indicated hereafter as Z.

All samples were further sulfated using H_2SO_4 1 N (15 ml/g) at room temperature, dried and calcined at 550 °C for 3 h. These catalysts are indicated hereafter as $SZ_{x\%}$-SBA and SZ.

2.2. Catalyst characterization

Small angle X-ray diffraction was performed using a Philips PW1729 diffractometer with Bragg–Brentano geometry θ–2θ and Cu $K\alpha$ radiation and a zero background quartz holder. The spectra were collected in the range of 2θ from 0.5 to 5° with step interval of 0.02°. The d_{100} value was calculated from Bragg's law, while a_0 for the hexagonal unit cell was calculated using the equation $a_0 = (2d_{100})/\sqrt{3}$.

X-ray photoelectron spectra (XPS) were measured at 45° takeoff angle relative to the surface plane with a PHI 5600 Multi Technique System that offers good control of the photoelectron takeoff angle (base pressure of the main chamber 2×10^{-10} Torr) [37,38].

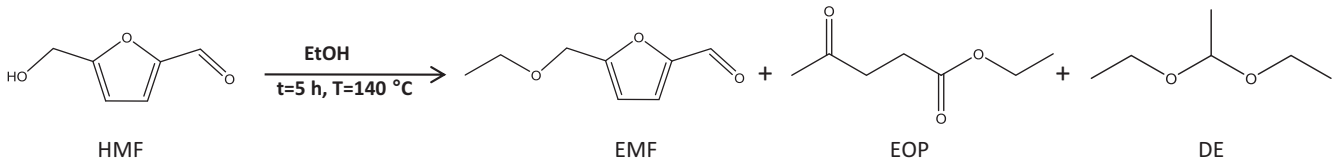

Scheme 1. Etherification of 5-(hydroxymethyl)furfural (HMF) to biodiesel additives.

Samples were excited with Al *K*α X-ray radiation using a pass energy of 5.85 eV. Spectra calibration was achieved by fixing the adventitious C1*s* peak at 285.0 eV. The XPS peak intensities were obtained after Shirley background removal. Structures due to the Al *K*α satellites were subtracted from the spectra before data processing. The instrumental energy resolution was ⩽0.4 eV. Spectra simulation was carried out by fitting the experimental profiles with symmetrical Gaussian peaks after subtraction of the background. This process involves data refinement, based on the method of least-squares fitting, carried out until there was the highest possible correlation between the experimental spectrum and the theoretical profile. The *R*-factor (residual or agreement factor), $R = [\Sigma(F_{obs} - F_{calc})^2/\Sigma(F_{obs})^2]^{1/2}$, after minimization of the function $\Sigma(F_{obs} - F_{calc})^2$, converged to *R* values ⩽0.02 [42].

The chemical composition was analyzed by energy-dispersive X-ray (EDX) analysis using an INCA Energy Oxford solid-state detector. Morphologies were examined through field emission gun scanning electron microscopy (FE-SEM) using a Zeiss SUPRA 55 VP microscope.

The surface areas were calculated from the Brunauer–Emmett–Teller (BET) equation and mesopore size distributions were calculated using the Barrett–Joyner–Halenda (BJH) model from the adsorption branch of the isotherms carried out at −196 °C on a Micromeritics ASAP 2010 sorption analyzer. Prior to the measurement, the samples were outgassed at 150 °C for 1 h to remove impurities. The average pore diameter and the cumulative pore volume were obtained from the distribution curve of the mesopore sizes, while micropore areas and volumes were calculated by the *t*-plot method.

The content of each species was evaluated by means of an Explorer X-ray Fluorescence spectrometer (BRUKER AXS) on solid samples. The instrument was previously calibrated in the energy range 0.11–0.60 keV, corresponding to wavelengths between 11.3 and 0.02 nm.

FTIR measurements on calcined samples were carried out on self-supporting wafers and the spectra were collected at a resolution of 2 cm^{-1} with a Perkin–Elmer FTIR spectrophotometer equipped with a MCT detector. The self-supporting wafers were prepared and activated under vacuum (10^{-4} Torr) for 1 h at 400 °C in an IR cell allowing in situ thermal treatments and pyridine dosage. Lewis and Brønsted acidic sites quantification was performed by integrating the areas underneath the bands at 1446 and 1547 cm^{-1}, respectively. The integrated molar extinction coefficients (IMEC) were calculated, according to Beer's law, by dosing pyridine at increasing concentrations over each sample under study, after evacuation at RT under high vacuum,

$$A = \varepsilon c D,$$

where *A* = absorbance; ε = molar extinction coefficient; *c* = concentration; and *D* = path length.

The ε value was obtained by plotting *A* vs. *c*, and more precisely the μmol_{py}, and assuming a constant *D* (since the sample is in pellet form and the thickness is always constant). Hence, Brønsted and Lewis acid sites were quantified using the equation

$$C_{\text{pyridine on X sites}} = \frac{\text{Area pellet} * \text{IA(X)}}{\text{IMEC(X)} * \text{Weight pellet}},$$

where $C = \mu mol\,g_{cat}^{-1}$ and IA(X) = integrated absorbance of the peak of the species X.

Diffuse reflectance UV–vis spectra (DR UV–vis) were obtained in air and under ambient conditions using a Jasco V-570 spectrometer equipped with an integrating sphere for solid samples. The reference was $BaSO_4$.

The morphology of samples was analyzed using a JEOL JEM 2010 TEM microscope operating at 200 kV.

2.3. Catalytic experiments

HMF etherification with ethanol was carried out in a Parr autoclave reactor (Teflon-lined) equipped with a Parr 4848 controller. Reaction tests were carried out at 140 °C for 5 h under autogenous pressure. The absence of interphase and intraphase gradients was checked by varying the stirring speed and the particle size until there was no effect on the reactant conversion [39]. As a general procedure, 2.5 mmol HMF was dissolved in 3.4 ml ethanol and put into the reactor containing the catalyst. The mixture was stirred at ca. 1500 rpm, and the progress of the reaction was followed by taking samples at regular periods and analyzed by Finnigan GC–MS.

3. Results

3.1. Characterization of host–guest phases

Fig. 1a shows the morphological aspect of the Z_{10}-SBA sample obtained by FE-SEM analyses. This material shows wormlike aggregates partially covered with flakes. A similar morphology, although slightly more nanostructured, is present on this material after the H_2SO_4 treatment (Fig. 1b). A similar effect is present also for the samples with 35 wt% zirconia loading (Fig. 1c and d, respectively), but also in zirconia alone, before and after sulfation (Fig. 1e and f, respectively). However, EDX mapping does not provide evidence for change in the Zr/Si distribution before and after sulfation, suggesting that there is only a local change of morphology due to solubilization/reprecipitation. Nevertheless, as shown later in the analysis of porosity and surface area, sulfation leads to a significant increase in the surface area of pure zirconia, but a minor effect when zirconia is on SBA-15.

Fig. 2 shows the low-angle ($0.5° < 2\theta < 4°$) XRD patterns of parent SBA-15 and ZrO_2-coated SBA-15 samples. For pure SBA-15, three distinct diffraction peaks appear at $2\theta = 0.92°$, 1.57°, and 1.80°, corresponding to (100), (110), and (200) planes, indicating the ordered mesoporous structure of SBA-15 with *p6mm* hexagonal symmetry [40]. The corresponding *d*-spacing of the (100) plane is 9.6 nm and the lattice parameter a_o is 11.1 nm, indicating that the support used to prepare the catalysts is well ordered at long range and contains mesopores in a hexagonal array.

The (100) XRD reflection is still observed for Z_{10}-SBA and SZ_{10}-SBA, but the position is shifted at slightly higher angles and the peak results broaden compared with that for pure SBA-15 and are attenuated in intensity. The (110) and (200) reflections are no longer detectable. Simulation of powder diffraction patterns of modified ordered mesoporous materials [41] indicates that

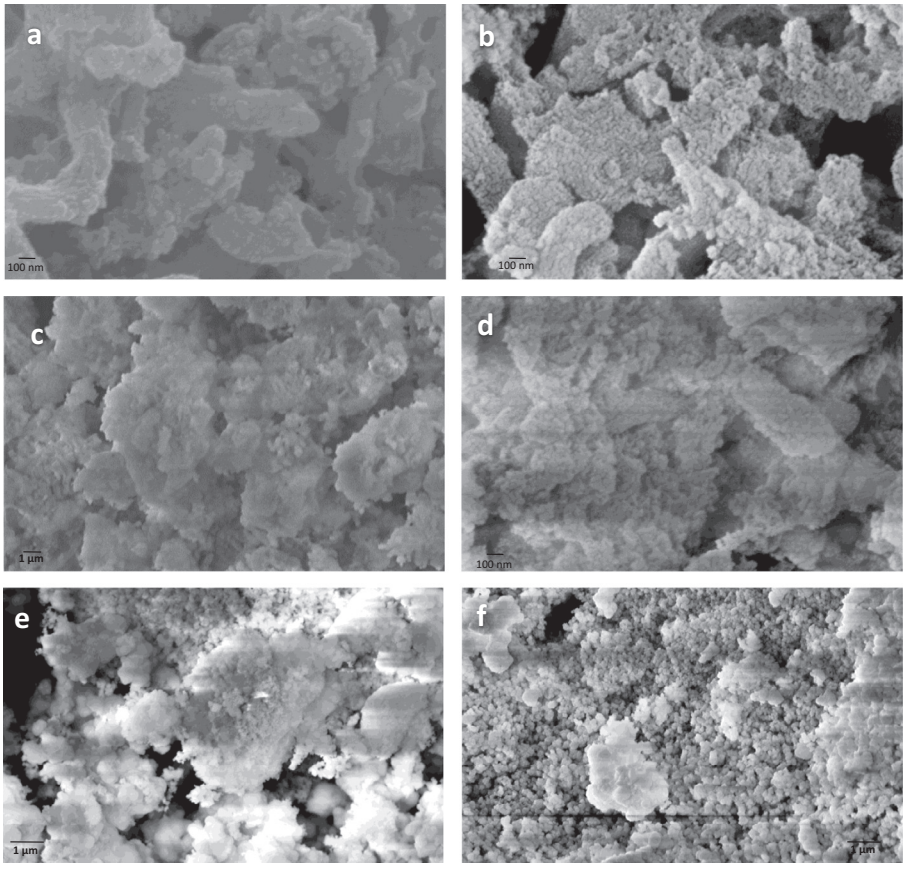

Fig. 1. SEM image of (a) Z_{10}-SBA, (b) SZ_{10}-SBA, (c) Z_{35}-SBA, (d) SZ_{35}-SBA, (e) Z, and (f) SZ at 100,000 magnifications.

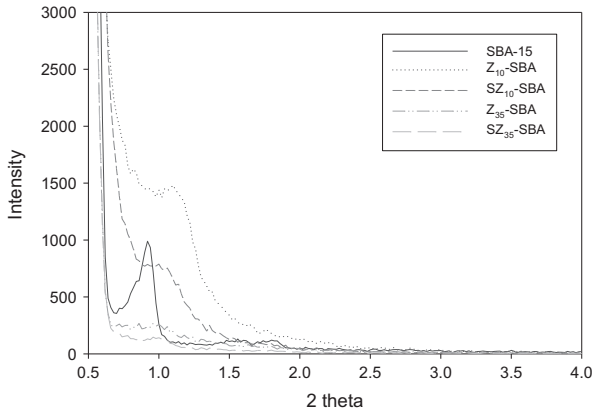

Fig. 2. Small-angle X-ray scattering of SBA-15, Z_{10}-SBA, SZ_{10}-SBA, Z_{35}-SBA, and SZ_{35}-SBA samples.

coating of inner walls by an oxide monolayer would shift the (100) reflection slightly to higher angles and cause depletion of the (110) and (200) reflections, but not influence the (100) reflection broadening and intensity. In contrast, the latter effect could be expected when oxide nanoparticles are present on the surface of SBA-15 particles, due to the broadening of the X-ray scattering contrast between the silica walls and the pore-filling material [42,43].

In the samples with higher zirconia loading (Z_{35}-SBA and SZ_{35}-SBA), the (100), (110), and (200) low-angle XRD reflections are no longer observable (Fig. 2). This could suggest that the ordered mesoporous structure is not preserved. However, for high oxide loading, X-ray scattering of inserted guest phase nanocrystals leads to strong reduction or even depletion of diffraction line intensities of SBA-15, even if the ordered mesoporous structure is still present [41]. The small-angle (SA) XRD intense reflection at about 0.9° corresponds to a (100) interplanar spacing of about 9.6 nm for a 2D hexagonal structure. The presence of a phase with different X-ray scattering, located inside the void structure of the mesoporous channels, interferes with the void/fill ordering responsible for this SAXRD reflection. Therefore, the absence of reflections in the low-angle XRD region of Z_{35}-SBA and SZ_{35}-SBA may not be indicative of the absence of ordered mesoporous structure, but in agreement with preferential location of zirconia inside the channels. In addition, it indicates that zirconia has not formed a smooth ZrO_2 layer on the internal walls of SBA-15, because in this case the preservation and even intensification of the (100) XRD reflection is expected.

Wide-angle XRD in the 10–60° region (not shown here) does not evidence the presence of crystalline zirconia phases, even for the higher zirconia loading. Therefore, zirconia is present either as an amorphous or as a crystalline phase, but with crystal size below about 3–4 nm, making them not detectable by XRD.

Fig. 3a shows the DR UV–vis spectra recorded in the region between 200 and 400 nm of Z_{10}-SBA and Z_{35}-SBA samples, together with those of pure SBA-15 and Z reference samples. No absorbance was observed for pure SBA-15, which is transparent in this region of the UV–vis spectrum. ZrO_2 (Z sample, tetragonal) shows instead an intense absorption below about 250 nm. This evidences the presence of a triplet absorption centered at 207, 214, and 227 nm. The first band corresponds to ligand-to-metal charge transfer from O^{2-} to highly dispersed Zr^{4+} ions [44]. The second mirrors a decrease in the dispersion of zirconia species and an increase in the coordination number, probably due to the

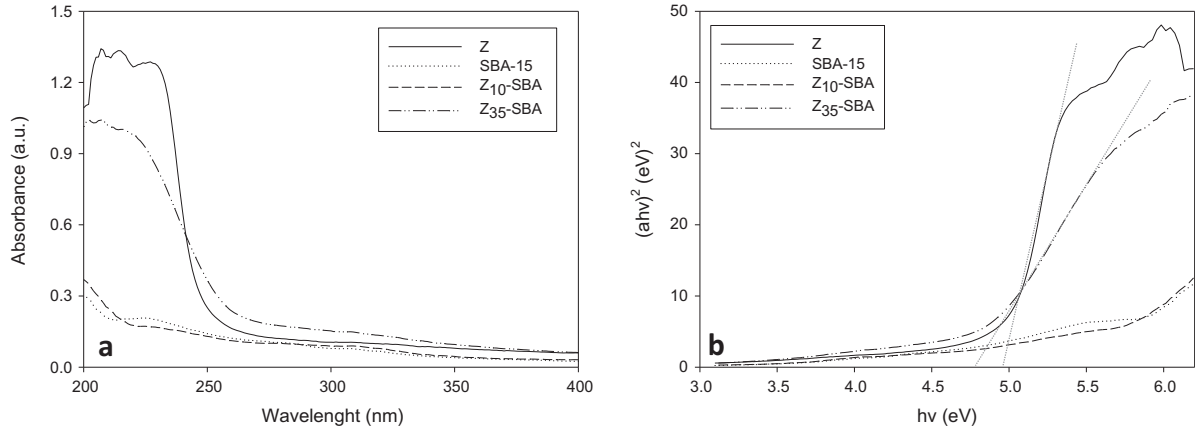

Fig. 3. (a) UV–vis spectra and (b) plot of $(ahv)^2$ vs. hv of the samples.

formation of Zr—O—Zr bonds. Finally, the band at 227 nm can be attributed to full connectivity of Zr—O—Zr linkages, revealing the aggregation of ZrO_2 species in bulk oxide [45]. In the Z_{35}-SBA sample, there is also intense absorption below 250 nm, but it is evident that the band at 227 nm is definitely weaker (compared to the other two bands) than in the pure ZrO_2 sample, indicating the presence of small zirconia nanocrystals in this sample. A broad band centered at about 300 nm may also be observed, giving rise to a change in the tail of the main band below 250 nm with respect to pure ZrO_2. This broad band, centered at about 300 nm (attributed to an intervalence band), together with the decrease in the relative intensity of the 227 nm band, is indicative of the presence of small and slightly distorted zirconia crystallites [46].

In the Z_{10}-SBA sample, the spectrum is essentially similar to that of pure SBA-15. Although the concentration of zirconia is about one-third of that present in Z_{35}-SBA, the zirconia phase should be clearly detectable when present in a form similar to that of pure zirconia (Z sample) or as in Z_{35}-SBA sample. However, it is known that for very small semiconductor nanoparticles (below than 2 nm), there is a blue shift in the band gap due to quantum confinement. In addition, these particles may be highly distorted, with a shift in the band-gap absorption below 200–210 nm. For this reason, the zirconia phase is apparently not detectable in the Z_{10}-SBA sample. This is in good agreement with the results of Liu et al. [45] on ZrO_2 on SBA-15 showing that an increase in the dispersion of zirconia leads to a shift from about 230 to around 200–210 nm of the ligand-to-metal charge transfer ($O^{2-} \rightarrow Zr^{4+}$).

Fig. 3b reports the absorption edge energy values (Eg) for the Z and Z_{35}-SBA samples quantified by the intercept of linear extrapolation to the hv axis. Pure zirconia gives an Eg value around 5 eV, in good agreement with the literature for the tetragonal phase, while the Eg value for Z_{35}-SBA is observed at about 4.8 eV, contrary to what is reported in the literature [47], where the red shift was attributed to the formation of Si—O—Zr linkages and surface Zr—OH groups. The observed blue shift in our case is instead consistent with the presence of small zirconia nanoparticles inside the SBA-15 channels.

3.2. Location of ZrO_2 in the SBA-15 support

Fig. 4 shows the TEM images of Z_{10}-SBA (4a, 4b) and Z_{35}-SBA (4c, 4d) samples. Both samples exhibit ordered arrays of mesopore with uniform pore size (around 9 nm), with the straight pore channels similar to those of parent SBA-15. This confirms that the absence of small-angle XRD reflections is not indicating a collapse of the ordered mesoporous array. TEM analysis also clearly shows two different distributions of ZrO_2 into SBA-15 support. While in Z_{10}-SBA the formation of ZrO_2 domains can be detected mainly out of the channels of SBA-15, only very limited ZrO_2 particles are present on the external surface of SBA-15 crystals in Z_{35}-SBA (see legend of Fig. 4). The zirconia phase in Z_{35}-SBA is thus mainly located inside the channels, while in Z_{10}-SBA it is predominantly present outside the SBA-15 channels.

The textural properties of the prepared catalysts are summarized in Table 1. Upon addition of ZrO_2 to the pure SBA-15, the specific surface area of these catalysts drops from 573 to 362 $m^2\,g^{-1}$ and to 405 $m^2\,g^{-1}$ for Z_{10}-SBA and Z_{35}-SBA, respectively, with a corresponding decrease in total pore volume from 1.67 to 1.18 $cm^3\,g^{-1}$ and 0.87 $cm^3\,g^{-1}$. The introduction of ZrO_2 into the SBA-15 matrix, affects the micropore volume and area values only for high ZrO_2 loading. In fact, no significant variation in the micropore volume and area values is observed (from 0.019 to 0.017 $cm^3\,g^{-1}$, and from 57 to 49 $m^2\,g^{-1}$, respectively) on passing from pure SBA-15 to Z_{10}-SBA, while both values significantly decline (0.006 $cm^3\,g^{-1}$ and 24 $m^2\,g^{-1}$) for Z_{35}-SBA. An analogous trend was observed for the corresponding sulfated samples. This is in good agreement with the indication of the other techniques that the location of zirconia is predominantly external for Z_{10}-SBA and predominantly internal to channels for Z_{35}-SBA.

The N_2 adsorption/desorption isotherms of SBA-15, Z_{10}-SBA, and Z_{35}-SBA are shown in Fig. 5. All the isotherms show the typical IV-type profile, according to the IUPAC classification, typical of mesoporous materials with pore size in the nanometric range. All samples show the formation of a monolayer for pressures below 0.4, while remarkable changes in the shape of the hysteresis loop profile, within a relative pressure range of 0.5–0.8, were observed after the introduction of ZrO_2 into the SBA-15 structure. For pure SBA-15, the sharp increase in the adsorbed N_2 volume is characteristic of capillary condensation in mesopores. The hysteresis loop of pure SBA-15, with vertical and parallel desorption and adsorption branches, is of type H1, characteristic of well-defined cylinder-like pores. Moreover, the sharpness of this jump indicates the uniformity of mesopore sizes. In the case of Z_{10}-SBA, the shape of the isotherm changes, giving rise to a predominantly H3-type hysteresis loop, with limiting adsorption at very high p/p_0. This behavior may be due to existence of nonrigid aggregates of platelike particles or assemblages of slit-shaped pores [48]. For the Z_{35}-SBA sample, the two branches of the hysteresis loop are nearly horizontal and parallel over a wide range of p/p_0, which results in an H4 hysteresis loop, generally associated with complex materials containing both mesopores and micropores. Finally, the observed step down in the desorption branches in Z_{10}-SBA and Z_{35}-SBA can be

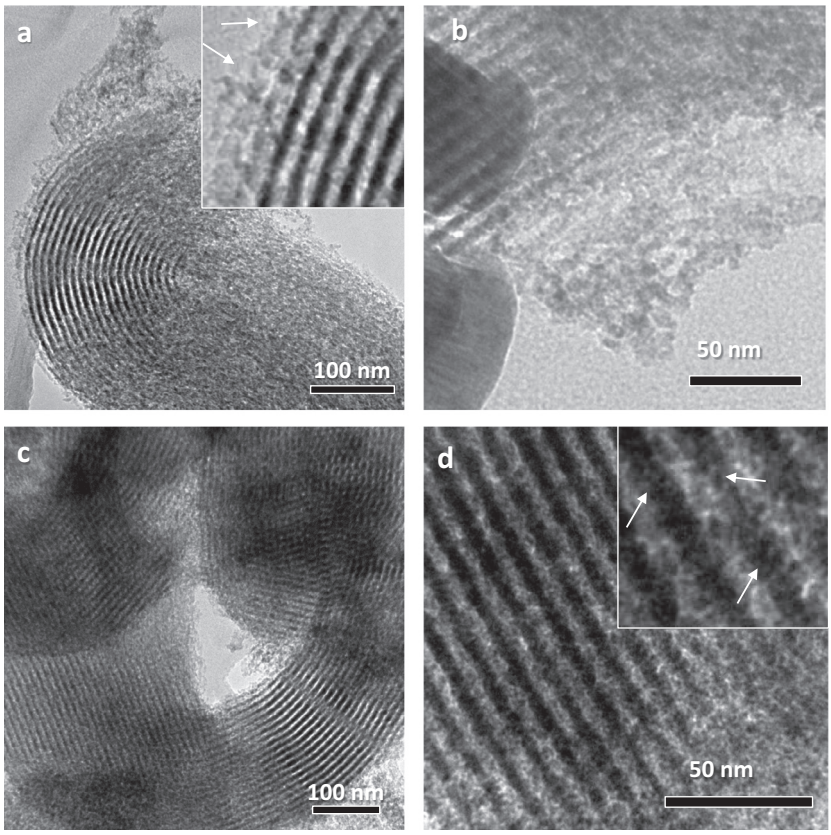

Fig. 4. HRTEM images of (a, b) Z_{10}-SBA and (c, d) Z_{35}-SBA samples. The insets in (a) and (d) show magnified images of the predominant locations of zirconia outside the mesoporous channels (Z_{10}-SBA) or inside the channels (Z_{35}-SBA). The arrows indicate zirconia nanoparticles determined by EDX local analysis.

Table 1
Textural properties of all the samples under study.

Samples	$S.A._{BET}$[a] (m^2/g)		V_{pore}[a] (cm^3/g)	d_{pore}[a] (Å)	$V_{micropor.}$[b] (cm^3/g)	$Area_{micropor.}$[b] (m^2/g)
	Exper.	Theor.				
SBA-15	573	–	1.67	78	0.019	57
Z_{10}-SBA	362	402	1.18	96	0.017	49
SZ_{10}-SBA	375	421	1.26	98	0.022	57
Z_{35}-SBA	405	578	0.87	63	0.006	24
SZ_{35}-SBA	396	557	0.91	67	0.004	24
Z	14	–	0.024	69	0.00031	0.86
SZ	94	–	0.089	38	0.0010	1.6

[a] Calculated using BET method.
[b] Calculated by t-plot method.

considered as further confirmation of the H3 and H4 character of the hysteresis loop. Analogous trends are observed for the corresponding sulfated samples (Fig. 1S).

There is thus a significant difference in the N_2 adsorption/desorption isotherms after loading of zirconia from those for parent SBA-15. It should be remarked that when zirconia is predominantly deposited in the form of a thin monolayer-type film over the inner walls of the SBA-15 channel, the H1 behavior (as for SBA-15) is expected. The concentration of zirconia nearly corresponds to a monolayer amount for Z_{35}-SBA and nearly one-third of a monolayer amount for Z_{10}-SBA. The significant change in N_2 adsorption/desorption isotherms after zirconia loading thus confirms the indication by other characterization techniques that with the preparation method adopted the zirconia has not reacted, if not in a minor amount, with the silanol groups to form monolayer-type species reconstructing the inner walls of the mesoporous SBA-15 channels. There is, however, a significant difference between the Z_{10}-SBA and Z_{35}-SBA samples (and the corresponding after sulfation). The N_2 adsorption/desorption isotherms are consistent with the indication on the volume of pores and micropores (Table 1), and other characterizations as well of the predominant location of zirconia external and internal to SBA-15 channels for Z_{10}-SBA and Z_{35}-SBA samples, respectively.

The trend of surface area is well consistent with this interpretation. The comparison between the experimental and theoretical S_{BET} for the Z_{35}-SBA sample (Table 1) indicates a decrease in the specific surface area proportional to the mass of the introduced zirconia. In the case of Z_{10}-SBA, an opposite trend was observed, consistent with the model that zirconia is located mainly at the external surface of SBA-15 or at the mouths of mesopore channels, giving rise to slit-shaped pores. At higher loadings, dual-step filling of pores can be hypothesized, where the first stage of deposition occurs at the mouths of mesopores and then continues inside the channel system with consequent filling of microporous corona

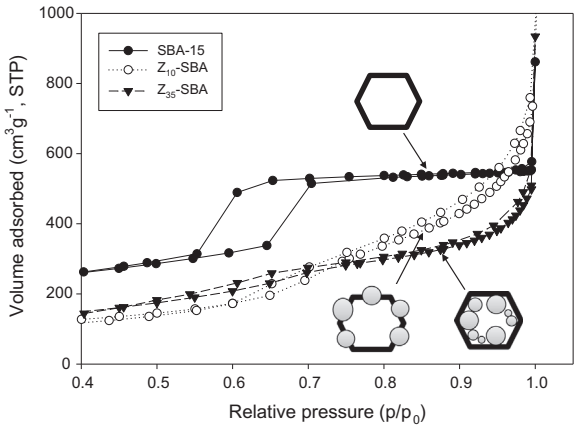

Fig. 5. N_2 adsorption–desorption isotherms for SBA-15, Z_{10}-SBA, and Z_{35}-SBA samples.

around the mesopores [19,25], as also confirmed by the decreasing trend of mean pore diameter with zirconia addition [49]. The driving force of the proposed filling mechanism can be considered as a combination of thermodynamic and kinetic effects, i.e., the tendency to minimize the surface strain energy and the concentration gradient of zirconia precursor inside and outside the SBA-15 pores during the synthesis process, respectively [50,51].

3.3. Surface elemental composition

The XPS characterization provides information on the bonding states and the surface elemental composition by accounting for the relevant atomic sensitivity factors [37,38]. Fig. 6 shows the XPS bands of C1*s*, Si2*p*, O1*s*, and Zr3*d* of the Z_{10}-SBA. The C1*s* XPS signal, omnipresent in all air-exposed materials, is due to the so-called adventitious carbon contamination and is currently used for XPS spectra calibration [37]. Both the energy position (285.0 eV) and the symmetric shape with no components at higher binding energy allow one to exclude the presence of carbonates.

The Si2*p* peak appears at higher energy (103.9 eV) than that expected for the SiO_2 phase (103.0 eV) and is due to the presence of silanols on the silica surface [52]. The Si2*p* binding energy was the same for the SZ_{10}-SBA and Z_{35}-SBA samples (Figs. 2S and 3S). This indicates that in both samples, a significant amount of silanols is still present, in agreement with the indications of the other characterization techniques that by this preparation method the reaction of zirconia with silanol groups is minimal.

The experimental XPS profile in the O1*s* binding energy region (black line) shows a rather unsymmetrical shape and was fitted using two Gaussian components at 531.8 (magenta line) and 533.1 eV (blue line), consistent with the ZrO_2 and SiO_2 phases, respectively [52,53]. The red trace superimposed on the experimental profile accounts for the sum of the two Gaussians. The green line represents the Shirley background. The 531.8 eV value is well above that obtained for the pure Z reference sample (530.6 eV) (Fig. 4S), and this is in agreement with the presence of Zr—OH species [53,54]. A similar unsymmetrical shape and binding energies have been observed for the O1*s* peak of Z_{35}-SBA (Fig. 3S), while the O1*s* peak of the SZ_{10}-SBA (Fig. 2S) does not show relevant asymmetries. This confirms the difference in the characteristics of zirconia nanoparticles when located external or internal to the SBA-15 mesoporous channels, suggesting also a difference in the acid–base properties.

The XPS spectrum of the Z_{10}-SBA in the Zr3*d* energy region shows several interesting features. They consist of the main $3d_{5/2}$, $3d_{3/2}$ spin–orbit components at 183.3 and 185.6 eV, respectively [54]. Both peaks are 0.7 eV shifted to higher binding energy with respect to the Z reference (Fig. 4S). This energy shift is due to the influence of the higher electronegativity of Si (1.8) than of Zr (1.4), thus confirming the presence of some acid–base interaction between silica and the ZrO_2 nanoparticles. Moreover, a broad satellite feature is shifted 14.5 eV from the main Zr $3d_{5/2}$ peak. In analogy to previous XPS results on pure and doped zirconia, this feature can be interpreted in terms of a shake-up phenomenon [53,54].

Binding energy values for the Zr3*d* states of Z_{35}-SBA show a small, but sizeable, decrease from those observed for the Z_{10}-SBA, the main $3d_{5/2}$ and $3d_{3/2}$ spin–orbit components being at 183.1 and 185.4 eV, respectively (Fig. 3S) [53]. This observed 0.2 eV shift indicates a slightly different environment for Zr in zirconia nanoparticles present in Z_{10}-SBA and Z_{35}-SBA samples, in agreement with their different locations and probably the presence of a more distorted environment in zirconia nanoparticles located inside the mesoporous SBA-15 channels.

The XPS atomic concentration analysis of the Z_{10}-SBA sample indicates a 0.056 Zr/Si atomic ratio, totally in agreement with the nominal Zr/Si value of 0.054 found for a reference 10/90 ZrO_2/SiO_2 wt% system. Moreover, this value is strongly reminiscent of 0.057, which is the intensity ratio between the 531.8/533.1 Gaussian components of the O1*s*. XPS being a surface technique able to probe a few (<10) nm of surface thickness, the near coincidence of the nominal and measured Zr/Si atomic ratios supports the hypothesis that at low loading, zirconia is located mainly at the external surface of SBA-15 or at the mouths of mesopore channels with no surface segregation [55–57]. The case of the Z_{35}-SBA, where the XPS atomic concentration analysis indicates a 0.10 Zr/Si atomic ratio vs. a 0.26 nominal value for a 35/65 ZrO_2/SiO_2 wt% system, is different. In this case, the location of the large majority of zirconia is inside the channel system at a depth not investigable with the XPS analysis. The only relevant observation for the SZ_{10}-SBA catalyst lies within the XPS atomic concentration analysis, which indicates a 0.029 Zr/Si atomic ratio. This value may suggest that the H_2SO_4 treatment causes some ZrO_2 to leave the surface and reach the channel system below the XPS probed depth.

In conclusion, the different physicochemical characterization techniques utilized agree in indicating that zirconia is predominantly present as small nanoparticles located external or internal to the mesoporous SBA-15 channels in Z_{10}-SBA and Z_{35}-SBA samples (and the corresponding ones after sulfation), respectively. Characterization techniques also indicate that the location of zirconia inside or outside of the channels determines some change in the characteristics of the oxide nanoparticles, reasonably related to strains induced from the growth of nanoparticles inside or outside the mesoporous channels. This reasonably reflects a change in the acid–base properties, as suggested by XPS. It should be noted, however, that mesoporous channels remain accessible in chemisorption experiments on the sample with the higher loading (Z_{35}-SBA), indicating that zirconia does not fully occlude the access to channels; i.e., the diameter of the zirconia particles inside the channels is less than the size of the channel itself. This is consistent with the observation of a diameter around 3 nm indicated by other characterization techniques and TEM observations as well. The size of zirconia nanoparticles located on the external surface is similar or slightly lower, except that there are very few with larger size, as indicated by TEM observation.

3.4. Surface acid properties

Surface acid properties of the samples were analyzed by FT-IR, using pyridine as a probe molecule, on the samples activated at 400 °C (Fig. 7). Pyridine has a diameter of 0.57 nm and is able to enter the pores of SBA-15, even if they are partially occluded by zirconia nanoparticles.

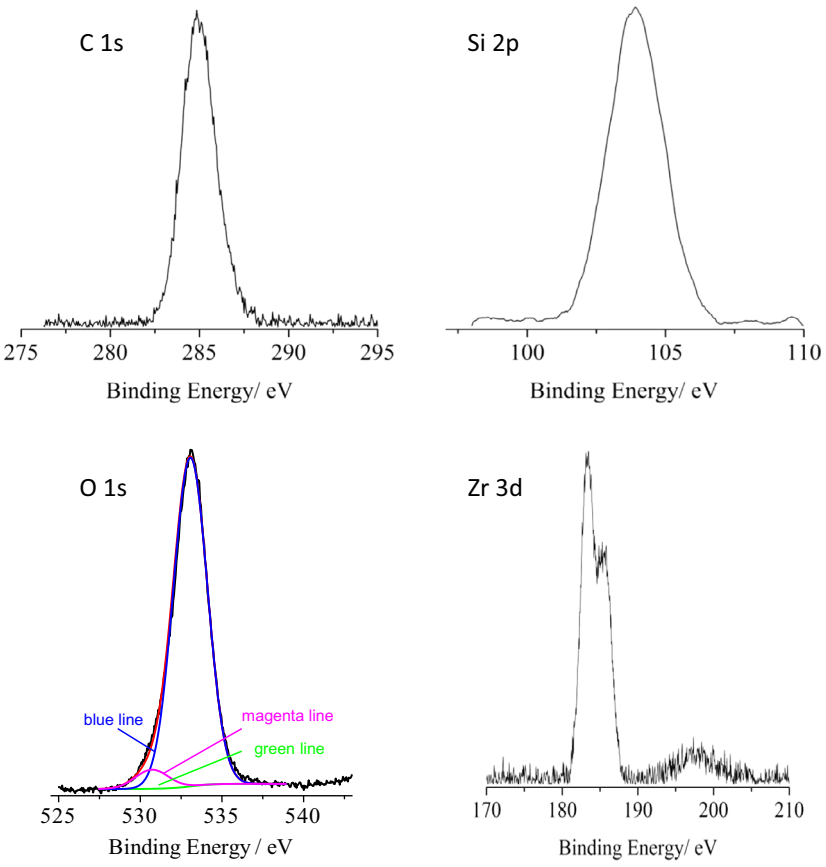

Fig. 6. Al *K*α-excited XPS of Z_{10}-SBA in the C1*s*, Si2*p*, O1*s*, and Zr3*d* binding energy.

In the region of OH stretching frequencies (3800–3500 cm^{-1}), all the SBA-15-containing samples display a band at 3750 cm^{-1}, related to isolated free silanols from the siliceous matrix (Fig. 7a). These species can be allocated both in the outer surface and within mesopores, where the distance between two silanols is high enough to let them almost unperturbed [58]. In pure SBA-15 this band appears intense, sharp, and symmetric, while in other samples it becomes slightly less intense and broader. Therefore, large amounts of silanols groups are still present, in agreement with other characterizations, but there is some perturbation of silanol groups, reasonably due to weak interaction with zirconia nanoparticles [37]. In parallel, a left shoulder of the silanol band at 3760 and a broad band at 3680 cm^{-1} emerge slightly. These features can be attributed to the Zr—OH and Zr—OH—Zr species, respectively [59,60], and become more intense with increasing ZrO_2 loadings.

The acidity of the catalysts was then probed by pyridine adsorption/desorption at RT. Fig. 7b shows the ring vibrational modes (1650–1400 cm^{-1}) of the irreversibly adsorbed portion of pyridine molecules, i.e., the part that is not removed by evacuation at room temperature. Interactions of pyridine, via the nitrogen lone-pair electrons with aprotic (Lewis) and protonic (Brønsted) acid sites, can be sensitively detected by monitoring ring vibration modes 8a and 19b. These modes, which appear at 1580 (8a) and 1439 (19b) cm^{-1} for gas-phase pyridine, undergo upward shifts upon coordination of the molecule with any type of acid site, Lewis or Brønsted [61].

Adsorption of pyridine resulted in strong reduction in all hydroxyl bands, consistent with the fact that the pyridine interacts with the hydroxyl groups both inside the pores and on the external surface (not shown here). Upon interaction of pyridine with Lewis acid sites, the band at 1580 cm^{-1} can be shifted to 1598 cm^{-1} or to a few wavenumbers depending on the strength of interaction with the acid sites. In parallel, the band at 1439 cm^{-1} undergoes a shift to 1446 cm^{-1}. In SBA-15, apart from the band at 1580 cm^{-1}, the features corresponding to the ring-stretching mode of pyridine-bonded Lewis acid sites appeared at 1598 (8a mode) and 1446 (19b mode) cm^{-1}. Similarly, ZrO_2-containing samples show strong IR absorption bands at wavenumber values in the range 1635–1600 cm^{-1} and at 1444 cm^{-1}, which are assigned (respectively) to the 8a and 19b modes of adsorbed pyridine forming Lewis-type adducts with coordinatively unsaturated Zr^{4+} ions. Moreover, in ZrO_2-containing samples, the intensity of the band at 1598 cm^{-1} (8b mode) decreases with zirconia loading, indicating that this band is probably associated with the presence of defective sites [62–64].

In parallel, smaller upward shifts are observed for the 19b mode after interaction with Brønsted acid sites, respectively from 1580 to 1638 cm^{-1} (8a) and from 1439 to 1545 cm^{-1} (19b), with the highest wavenumbers (in each group) corresponding to the combined C—C stretching and N—H bending modes of protonated pyridine. Finally, the band at 1490 cm^{-1} (19a mode) results from a joint contribution of Lewis and Brønsted acidic sites [62]. In particular, such features were prominent in sulfated materials (SZ_{10}-SBA and SZ_{35}-SBA), with a slight increase with ZrO_2 loading. Additionally, in sulfated samples, a gradual red shift of the band from 1446 to 1438 cm^{-1} was observed [59], especially for the SZ sample, due to the strengthening of the Lewis acid sites, as a consequence of the formation of Brønsted sites.

According to Emeis [65], the determination of the IMEC (integrated molar extinction coefficients) for Lewis and Brønsted acidic sites quantification was made using the integrated areas

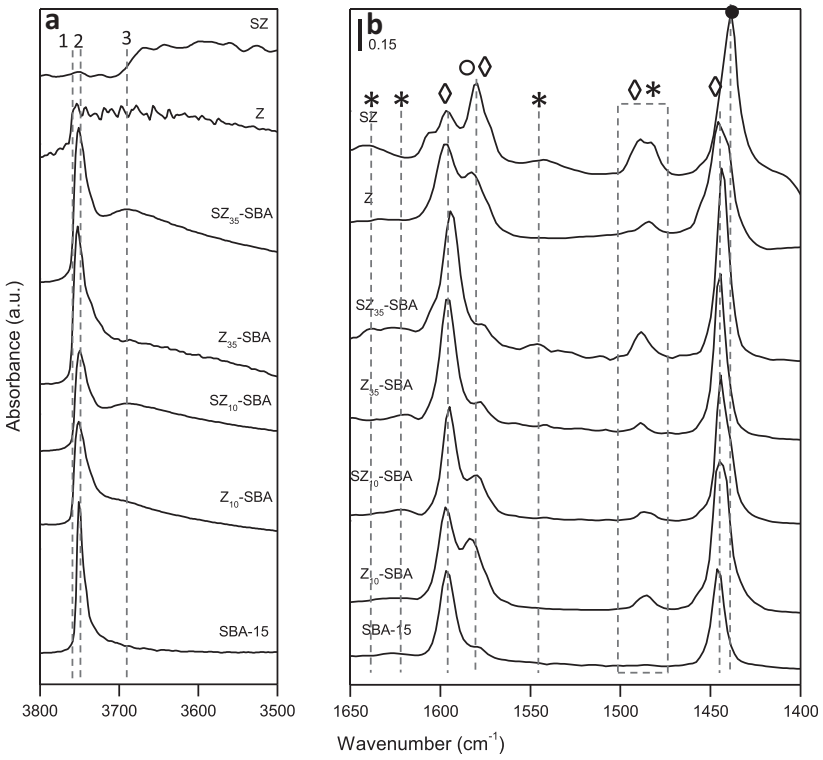

Fig. 7. FT-IR spectra of samples (a) before and (b) after pyridine adsorption at RT; samples were previously outgassed at 400 °C for 1 h under vacuum. (*) symbols indicate bands attributed to PyH^+ species; (◇) symbols are related to H-bonds to weak acid Brønsted or Lewis sites; finally, (•) symbols correspond to bands with reinforcement of acidic sites, (○) physisorbed gas phase pyridine.

Table 2
Acid amount of Brønsted and Lewis acid sites calculated from the pyridine adsorption spectra collected at RT, after outgassing under vacuum.

Samples	μmol Lewis acidity (1446 cm^{-1})	μmol Brønsted acidity (1540 cm^{-1})
Z_{10}-SBA	14.8	0
SZ_{10}-SBA	19.8	0.6
Z_{35}-SBA	17.9	0
SZ_{35}-SBA	28.1	1.8
Z	3.5	0
SZ	32.0	3.6

underneath the bands at 1446 and 1547 cm^{-1}, respectively. The values obtained by independent experiments following the Emeis procedure were 1.67 and 2.85 cm^{-1} μmol^{-1} (confidence limit of 95%) for $IMEC_{Brønsted}$ and $IMEC_{Lewis}$, respectively. Using these IMEC factors, and normalizing the value to the same film thickness by considering the skeletal vibrations of SBA-15 (added in a specific amount by mechanical mixing in the case of Z and SZ samples), it is possible to quantify the concentration of Brønsted and Lewis acidity in the different samples before and after sulfation (Table 2).

The sulfation of zirconia (Z) leads to a significant increase of Lewis and Brønsted acidity, especially the former, as expected. Although there is still debate on the nature of the sites responsible for this effect, it is often indicated that sulfation generates on the surface a sulfate species having two covalent SO double bonds bound to a metal cation [59,66,67]. The strong acidity derives from the tendency to lose the double bond character or decrease the bond order of SO by an electronic shift from a basic molecule adsorbed onto the sulfate complex, with an intimate relationship between the generation of acidic properties and the dispersion of active sites. Hino et al. [66] assessed that the Lewis acid strength of Zr^{4+} becomes remarkably greater by the inductive effect of S=O in the metal–sulfate complex. In the presence of water, these Lewis acid sites may be converted into Brønsted ones via proton transfer, as confirmed by Bolis [68]. They almost always consist of polysulfate species comprising three or four oligomers with two ionic bonds of S—O—Zr, in addition to coordination bonds of S=O with Zr.

Hence, the definition of the edge between Lewis and Brønsted acidity is crucial. Tanabe et al. [69] suggested an interconversion of Brønsted into Lewis by interaction with hydrocarbons or water, while Ward et al. [70] concluded that the proton of a hydroxyl group bonded to Zr is strengthened by the presence of a SO species chelated to an adjacent Zr atom, by an electron inductive effect. Vedrine et al. [71] observed that the generation of active Lewis sites occurs not on the metal, but only on S atoms. Both findings would suggest that sulfation not only reinforces Brønsted acidity, but also itself creates Lewis acid sites [70,72,73].

Fig. 8 shows the trend for Lewis (a) and Brønsted (b) acid sites, as a function of the concentration of zirconia on SBA-15.

Assuming the presence of mechanical mixing between zirconia and SBA-15, linear dependence on the concentration of zirconia in Z/SBA-15 samples is expected (lines in Fig. 8). While for Brønsted acidity there is reasonably good linearity of the number of acid sites from the loading of zirconia, there is a significant deviation for the Lewis acidity in both Z_{10}-SBA and Z_{35}-SBA samples (before and after sulfation), showing a significantly larger number of Lewis acid sites.

If the effect were a simple dispersion effect, leading to smaller (supported) particles, an equivalent effect on the concentration of Brønsted acid sites would expected. In addition, the effect of sulfation in enhancing the number of Lewis acid sites would be similar. In pure zirconia, sulfation increases the number of Lewis acid sites by a factor of about 9. In SZ_{10}-SBA, this factor is about 1.3, and in SZ_{35}-SBA, about 3.6. Therefore, sulfation enhances the number of

Lewis acid sites as in pure zirconia, but the zirconia nanoparticles on SBA-15 already show a significant larger number of Lewis acid sites, with thus a reduced enhancement factor after sulfation. It could be also noted that the location of zirconia particles on or within the SBA-15 particles influences this enhanced Lewis acidity, before and after sulfation.

3.5. Catalytic activity

The catalysts, before and after sulfation, were studied in HMF etherification with ethanol, which was used as a model reaction to analyze the acidic characteristics of the samples, besides its specific interest in producing biodiesel components, as indicated in Section 1. In the reaction conditions used for the catalytic tests (140 °C, autogenous pressure, ethanol as reactant and reaction medium), the main reaction products observed were 5-(ethoxymethyl)furan-2-carbaldehyde (EMF), 1,1-diethoxyethane (DE), and ethyl 4-oxopentanoate (EOP). EMF and EOP derive from HMF conversion, while DE derives from the reaction of ethanol with the small amount of acetaldehyde in equilibrium with it, favored by the presence of acid sites on the catalysts [74]. Other by-products were also detected in traces, such as 2,5-furancarboxaldehyde, 2,5-dimethylfuran, 5-(methyl)furan-2-carbaldehyde, ethyl formate, ethyl acetate, diethyl ether, and others in smaller amounts. EMF and EOP are the main products deriving from HMF and thus attention is focused here on their formation, in addition to the rate of HMF depletion (Table 3).

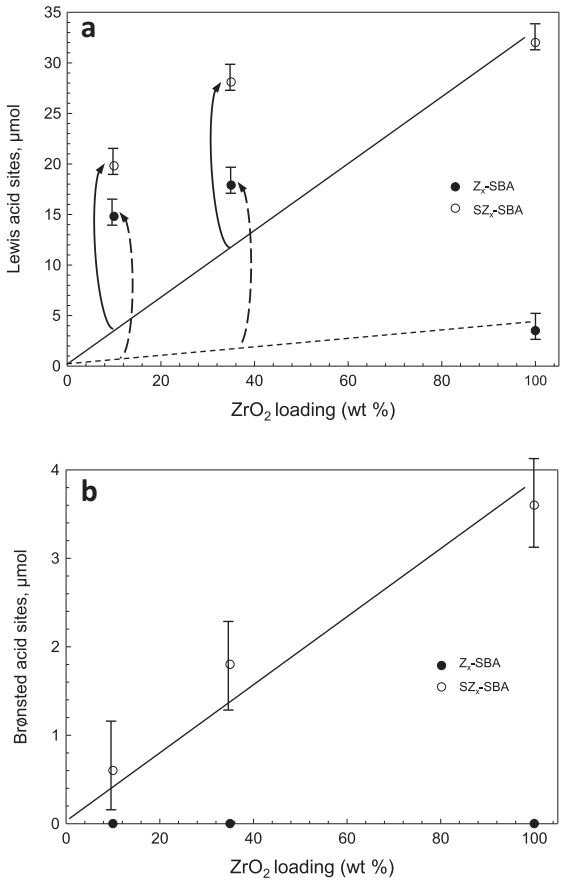

Fig. 8. Lewis (a) and Brønsted (b) acid sites, calculated from the pyridine adsorption spectra collected at RT, after outgassing under vacuum, as a function of zirconia loading, before and after sulfation. The arrows indicate the acidity intensification with respect to that expected in the case of a mechanical mixture between pure zirconia and SBA-15.

The catalytic tests being made in ethanol as reactant and solvent, the rate of HMF conversion may be described as a pseudo-first-order equation, e.g., independent of ethanol concentration. By applying the reactor model for a batch well-stirred reactor, it is possible to derive from the data on HMF conversion as a function of time on stream the pseudo-first-order rate constant of HMF depletion (k_{HMF}) for the various catalysts. The results are summarized in Fig. 9, which also reports for better visual comparison the data on the number of total acid sites in the catalyst (determined by pyridine chemisorption) as a function of the amount of zirconia, and the lines represent the expected linear relationship (e.g., as a mechanical mixture of ZrO_2 and SBA-15 would be present).

For pure zirconia, before and after sulfation, it may be evidenced that there is good correspondence between increase of k_{HMF} and increase of the number of total acid sites. It is thus reasonable to attribute the conversion of HMF to the presence of total acid sites. When this relationship is analyzed for Z_{10}-SBA and Z_{35}-SBA samples (before and after sulfation), an effect similar to that discussed before may be evidenced for the dependence of the number of Lewis acid sites on the zirconia loading. In fact, both the rate constant and the total acid sites are higher with respect to that expected for a linear relationship but the deviation from the linearity is less pronounced in the case of k_{HMF} with respect to that observed for total acid sites.

From Fig. 9, it is also notable that the reaction rate does not change proportionally to the concentration of ZrO_2: in fact, there is an incremental factor of 1.15 passing from Z_{10}-SBA to Z_{35}-SBA, and of 1.33 passing from SZ_{10}-SBA to SZ_{35}-SBA, while the concentration of zirconia triples. This suggests that the specific activity in HMF conversion (per amount of zirconia) of Z_{10}-SBA samples (before and after sulfation) is significantly higher than that of Z_{35}-SBA samples (before and after sulfation).

In fact, the specific space–time yields (STY, calculated as amount in g of the product formed per h and per g of zirconia present in the sample) of the two main reaction products, EMF and EOP, over all the catalysts are reported in Fig. 10.

In all samples, before sulfation, only EMF is detected, with a specific activity per amount of zirconia about three times higher in Z_{10}-SBA (0.41 g h^{-1} g^{-1}_{ZrO2}) than per amount of Z_{35}-SBA (0.14 g h^{-1} g^{-1}_{ZrO2}) and 11 times higher than per amount of pure zirconia (0.04 g h^{-1} g^{-1}_{ZrO2}). After sulfation, both EMF and EOP are detected, with enhancement of EMF production by a factor of 5–6 (2.46, 0.80, and 0.22 g h^{-1} g^{-1}_{ZrO2} for SZ_{10}-SBA, SZ_{35}-SBA, and SZ, respectively). These results are consistent with those commented on before regarding the specific concentration of Lewis acid sites per amount of zirconia in the catalyst.

In contrast, the specific STY of EOP is nearly constant (per g of zirconia), ranging from 0.26 g h^{-1} g^{-1}_{ZrO2} for SZ_{10}-SBA, 0.21 g h^{-1} g^{-1}_{ZrO2} for SZ_{35}-SBA, to 0.17 g h^{-1} g^{-1}_{ZrO2} for SZ. Horvat et al. [75] reported that a reinforcement of Brønsted acidity after sulfation may enhance the catalytic degradation of HMF to levulinic acid and the

Table 3
Catalytic performance in the etherification of HMF with EtOH of zirconia-based catalysts.

Samples	Conversion (%)	Space time yield (mmol/h/g_{cat})	
		EMF	EOP
SBA-15	43	0.117	–
Z_{10}-SBA	52	0.266	–
SZ_{10}-SBA	95	1.597	0.181
Z_{35}-SBA	65	0.273	–
SZ_{35}-SBA	100	1.403	0.403
Z	51	0.240	0.007
SZ	100	1.455	1.160

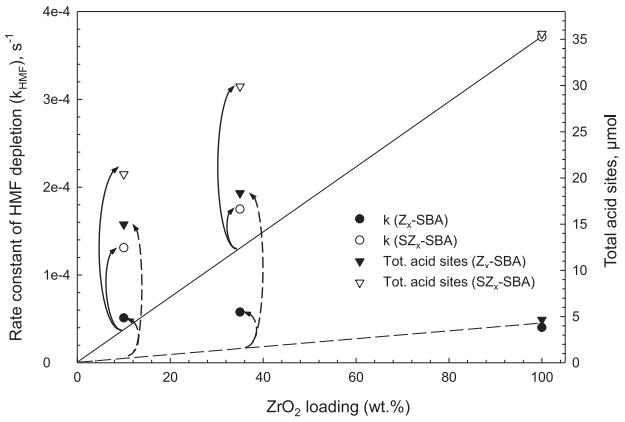

Fig. 9. Relationship between the rate constant of HMF conversion and the concentration of zirconia in Z_x-SBA samples, before and after sulfation. For comparison, data on the number of total acid sites are also reported. The arrows indicate the rate constant or acidity intensification with respect to that expected in the case of a mechanical mixture between pure zirconia and SBA-15.

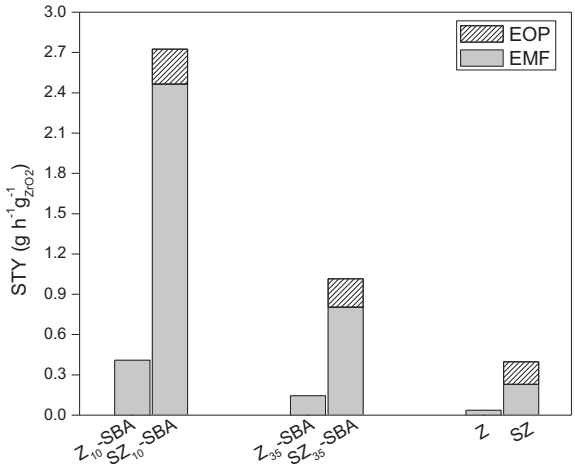

Fig. 10. STY normalized to ZrO_2 content of Z_{10}-SBA, SZ_{10}-SBA, Z_{35}-SBA, SZ_{35}-SBA, Z, and SZ.

subsequent esterification reaction with ethanol to give EOP. Che et al. [76], studying EMF conversion into EOP over $H_4SiW_{12}O_{40}$ catalysts, highlighted a pathway of EMF ethanolysis over Brønsted acid sites to form EOP. Similarly, in our systems, in the presence of Lewis acidity alone, attributable to surface Zr^{4+} sites, the insertion of the ethoxy group into a HMF molecule can be favored by the formation of highly polarized bonds between the substrate and the Lewis site and the possibility of delocalizing the charge all over the furanic ring. When Brønsted acidity is also present, both HMF and EMF conversion may occur, passing through a common intermediate (*, 2-ethoxy-5-methylidene-2,5-dihydrofuran-2-carbaldehyde) (Scheme 2).

A simplified triangular reaction network (valid for ethanol in large excess, as under our experimental conditions, where ethanol is the solvent of reaction) may thus be presented, where the rates of the different reactions will depend on the number of medium–strong Brønsted and Lewis acid sites (detectable by pyridine adsorption) (Scheme 3).

In agreement, we observed on sulfated samples the presence of Brønsted acidity, with the number of these sites linearly depending on the concentration of zirconia (Fig. 8b). As a consequence, a good linear relationship could be observed between the rate of EOP formation and the number of Brønsted acid sites in the sample (Fig. 11). For EMF, no clear relation could be observed with Lewis acid sites detectable by pyridine adsorption, and two distinct behaviors are observed for unsulfated and sulfated catalysts.

Then, considering this simplified reaction network and pseudo-first-order reactions (ethanol is in large excess), the rates of reaction may be written as

$$r_B = (k_1 \cdot L)C_A - (k_3 \cdot B)C_B,$$
$$r_C = (k_2 \cdot B)C_A + (k_3 \cdot B)C_B,$$

where A = HMF, B = EMF, and C = EOP, and L and B represent the concentrations of Lewis and Brønsted acid sites, respectively, as determined from pyridine adsorption experiments. The integration of these reaction rates for the well-stirred batch reactor model leads to the equation for the concentration of EMF,

$$C_B = \left(\frac{k_1^* C_A}{k_3^* - k_1^*}\right)\left(e^{-k_1^* t} - e^{-k_3^* t}\right), \quad (1)$$

where t is the reaction time and

$$k_1^* = (k_1 L + k_2 B),$$
$$k_3^* = (k_3 B).$$

Fig. 12 report, the formation of EMF for Z_{35}-SBA samples before and after sulfation according to the above simplified model, where symbols are the experimental values and lines are calculated considering the concentrations of Lewis and Brønsted acid sites reported in Table 2. For the Z_{35}-SBA sample, the calculated values of k_1^* and k_3^* are 4.60×10^{-6} and 0, respectively, while for the SZ_{35}-SBA sample, these values are 1.57×10^{-4} and 7.00×10^{-5}, respectively. k_2^* is zero for Z_{35}-SBA and 1.50×10^{-4} for SZ_{35}-SBA. Is it to be remarked that the objective is not a kinetic analysis, but to evidence only that a simple model such as that discussed above, based on the different role of Lewis and Brønsted acid sites in the various steps and their quantification by pyridine chemisorption, gives a reasonably good description of the experimental behavior observed before and after sulfation.

4. Discussion

All characterization results (TEM, XRD, BET, UV–vis, and XPS) agree in indicating that zirconia is present in Z_{10}-SBA samples (before and after sulfation) mainly in the form of zirconia nanoparticles (not detectable by XRD) deposited on the external surface of the ordered hexagonal mesoporous structure of SBA-15. The particles are instead predominantly located inside the mesoporous channels in Z_{35}-SBA (before and after sulfation), in the form of nanoparticles not preventing diffusion of molecules inside the channels. No evidences were found instead of the reaction of zirconia with the silanol groups of mesoporous silica, present mainly inside the channels, to form mono- or polynuclear zirconia species, leading to a reconstruction of the "corona" area in the SBA-15 channels. This is reasonably attributable to the specific conditions of preparation (urea hydrolysis). In fact, the synthesis is based on the change of pH induced by urea hydrolysis on increasing the temperature (90 °C), which results thus in a homogeneous deposition of zirconium hydroxide that transforms later to the zirconia oxide nanoparticles. Due to the different hydrophilic local characteristics of silica inside or outside the mesoporous channels, related to the specific mechanism of formation of mesoporous silica materials, it is likely that local urea concentration inside or outside the channels is different. This is one of the possible reasons, although not the only one explaining why a different location of zirconia nanoparticles is observed in Z_{10}-SBA and Z_{35}-SBA samples. As commented on in Section 1, this effect in still under investigation, but not relevant here, because the main objective in this work was to use these two samples as models to understand the

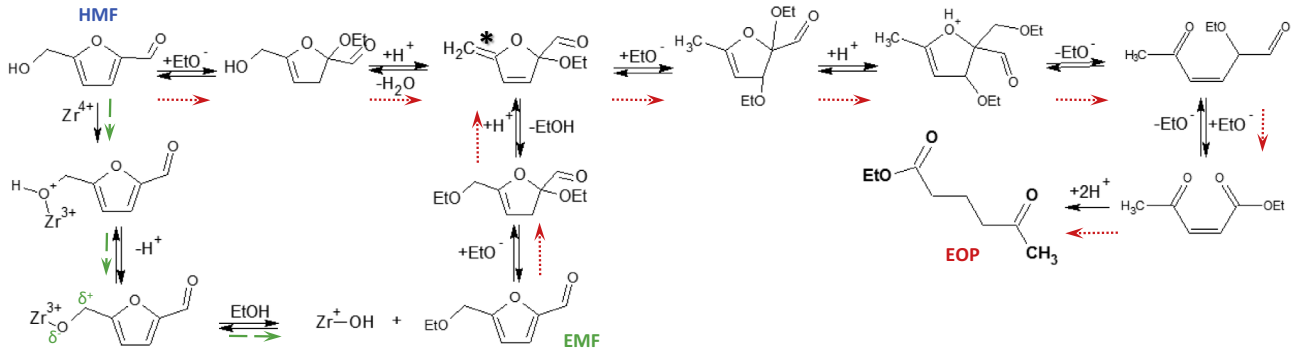

Scheme 2. Proposed reaction mechanism: HMF conversion pathway on Brønsted (red-dotted arrow) and Lewis (green-dashed arrow) sites.

Scheme 3. Simplified reaction network for conversion of HMF to EMF and EOP, with indication of the roles of Lewis (L) and Brønsted (B) acid sites in the different reaction rates.

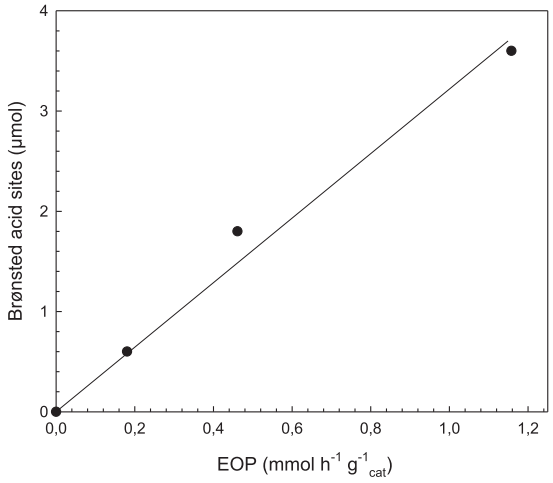

Fig. 11. Correlation between EOP productivity and Brønsted acidity.

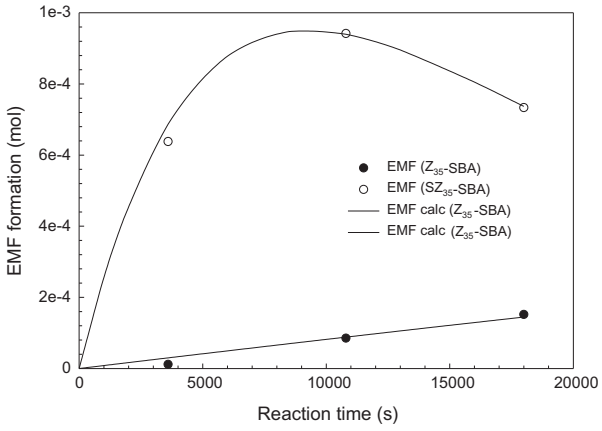

Fig. 12. Formation of EMF as a function of time on stream for Z_{35}-SBA samples before and after sulfation. Symbols are the experimental values, while the lines are calculated according to the simplified kinetic model described in the text, based on the concentrations of Lewis and Brønsted acid sites in the various reactions and their quantification by pyridine chemisorption.

influence of the location of zirconia inside or outside the mesoporous channels. Nevertheless, the different expected precipitation rates of zirconium hydroxide inside or outside the channels could explain why the characteristics and specific reactivity of the zirconia particles, before and after sulfation, are different depending on location.

However, it is interesting to investigate this difference and, as far as we know, there are no clear studies on this aspect.

We have thus focused the analysis on the quantification of medium–strong Brønsted and Lewis acidity by pyridine chemisorption monitored by IR spectroscopy and on the analysis of the catalytic behavior in HMF etherification using ethanol as solvent and co-reactant. Although it was earlier indicated that this or analogous reactions depend on the presence of Brønsted and Lewis acidity, it was never attempted to quantitatively correlate the number of acid sites detected with the catalytic behavior. The results discussed in this work evidence that a good correlation exists between the number of Lewis acid sites and the rate of direct EMF formation, and between the number of Brønsted acid sites and the rate of EOP formation, which is produced (through a series of reaction intermediates) directly from HMF or as consecutive conversion of EMF (Scheme 2). A simplified triangular reaction network, with the rate of EMF depending on the concentration of Lewis acid sites and the rates of EOP formation (parallel and consecutive) on the concentration of Brønsted acid sites, describes the observed behavior reasonably well. Therefore, both the trend of the number of acid sites determined by pyridine chemisorption and the catalytic performance are indicative of possible changes in the features of zirconia nanoparticles depending on the location inside or outside the silica mesoporous channels.

While the number of Brønsted acid sites (formed after sulfation) depends nearly linearly on the concentration of zirconia in SBA-15 (Fig. 8b), a marked deviation is observed for Lewis acid sites (Fig. 8a). The same conclusion could be derived from the analysis of the dependence of the catalytic activity on Lewis (Fig. 9)- or Brønsted (Fig. 11)-acid-site-promoted reactions. A possible interpretation is that there is a simple effect of better dispersion of zirconia nanoparticles, due to the support effect of SBA-15. However, this interpretation (e.g., no modification of zirconia nanoparticle characteristics, but only a higher specific surface area due to smaller nanoparticles) would imply that the same effect should be present also for Brønsted acidity. This not being the case, there must be some promotional effects, which enhance the relative number of Lewis acid sites (particularly after sulfation) in supported nanoparticles with respect to equivalent bulk oxide, and in turn the catalytic reactivity.

In particular, the effect superimposed by the sulfation treatment seems to be crucial, not only for the generation of Brønsted acidity, but also for the reinforcement of Lewis acidity already present and the creation of new active centers that take part to the reaction(s) pathways. Hence, one could expect that this promotional effect would depend purely on the ZrO_2 loading. Instead it has been observed that this additional effect is more pronounced when zirconia particles are located outside the mesoporous channels (Z_{10}-SBA), and less so when they are predominantly present inside the channels (Z_{35}-SBA). A close comparison between the dependence of the concentration of total acid sites and of the rate constant of HMF depletion on the zirconia loading (Fig. 9) shows that the trend and the effect of sulfation are quite similar, but the enhancement factor in terms of the rate constant is less pronounced than that observed for the number of acid sites. We define here as "enhancement factor" the increase in the rate constant or in acidity relative to the theoretical value expected for a corresponding mixture of pure zirconia and SBA-15. This different enhancement factors could be interpreted by assuming that under the dynamic conditions of catalytic tests, differently from the equilibrium conditions in pyridine chemisorption tests, part of the Lewis acid sites may be not accessible. However, this interpretation is in contrast with the observation of exactly the same enhancement effect independent of the location of zirconia nanoparticles outside or inside the mesoporous channels (Fig. 9).

The more reasonable interpretation is thus that only part of the Lewis acid sites, probably those with higher acid strength, are active in the catalytic reaction, while both medium- and higher-acid-strength Lewis sites are detected by pyridine chemisorption. Although this aspect requires more studies to be fully confirmed, the consequence of this interpretation is that the location of zirconia nanoparticles outside the mesoporous channels leads to a larger number of Lewis acid sites and as a consequence to higher specific catalytic activity in relation to location within the mesoporous channels (Figs. 9 and 10). The catalytic results themselves may suggest that lower reactivity of nanoparticles inside the channels may be due to the presence of some diffusional limitations, but the parallel effect observed on the concentration of Lewis acid sites and the good correspondence observed in all samples (including unsupported ones) between number of acid sites and catalytic behavior suggests that the effect is rather due to an intrinsic change in the physicochemical and reactivity properties of zirconia nanoparticles, when located inside or outside the mesoporous channels, as confirmed by most of the characterization data here presented.

5. Conclusions

In conclusion, this work has shown for the first time, as far as we know, (i) the existence of a quantitative relationship between the numbers of Lewis and Brønsted acid sites and their catalytic performance in HMF etherification with ethanol, a reaction of industrial relevance for the production of biodiesel additives; (ii) the influence of the location of zirconia nanoparticles inside or outside the mesoporous channels of SBA-15 on the specific reactivity in this reaction; and (iii) the effect of sulfation treatment on the changes in the relative distribution and reactivity of the catalytically active centers, with consequences for the activation of parallel reaction pathways. Although further studies are necessary to go into depth on the reasons for the differences of catalytic behavior depending on zirconia location, we believe that these results could open new perspectives of research in the field of oxide/mesoporous silica materials, an area of increasing interest for catalysis and beyond. Although part of the reasons are also related to the specific method of preparation adopted (urea hydrolysis), this is also a method often utilized to prepare catalysts and oxide/SBA-15 composites as well. By the use of different characterization techniques, it has been clearly proven that the number and the reactivity of acid sites, both Lewis and Brønsted, are not related only to a pure physical dispersion factor as commented on above, but rather also to the formation of different crystal nanoshapes and defects of strains, which in turn are governed by oxide location in the SBA-15 support.

Acknowledgments

This work was realized with the partial financial support of BIOFUR (biopolymers and biofuels from furan based building blocks), Marie Curie IAPP Contract 324292, and PRIN 2010-11 project, "Innovative processes for the conversion of algal biomass for the production of jet fuels and green diesel."

Appendix A. Supplementary material

Supplementary data associated with this article can be found, in the online version, at http://dx.doi.org/10.1016/j.jcat.2014.12.001.

References

[1] D. Stošić, S. Bennici, J.-L. Couturier, J.-L. Dubois, A. Auroux, Catal. Commun. 17 (2012) 23–28.
[2] A. Osatiashtiani, A.F. Lee, D.R. Brown, J.A. Melero, G. Morales, K. Wilson, Catal. Sci. Technol. 4 (2014) 333–342.
[3] R. Kourieh, V. Rakic, S. Bennici, A. Auroux, Catal. Commun. 30 (2013) 5–13.
[4] M. Watanabe, Y. Aizawa, T. Iida, R. Nishimura, H. Inomata, Appl. Catal. A: Gen. 295 (2005) 150–156.
[5] F. Chen, X. Meng, F.S. Xiao, Catal. Surv. Asia 15 (2011) 37–48.
[6] K. Arata, Green Chem. 11 (2009) 1719–1728.
[7] M.K. Patil, A.N. Prasad, B.M. Reddy, Curr. Org. Chem. 15 (2011) 3961–3985.
[8] R. Weingarten, G.A. Tompsett, W.C. Conner Jr., G.W. Huber, J. Catal. 279 (2011) 174–182.
[9] R. Otomo, T. Yokoi, J.N. Kondo, T. Tatsumi, Appl. Catal. A: Gen. 470 (2014) 318–326.
[10] G.S. Foo, D. Wei, D.S. Sholl, C. Sievers, ACS Catal. 4 (2014) 3180–3192.
[11] J. Luo, J. Yu, R.J. Gorte, E. Mahmoud, D.G. Vlachos, M.A. Smith, Catal. Sci. Technol. 4 (2014) 3074–3081.
[12] P. Lanzafame, D.M. Temi, S. Perathoner, G. Centi, A. Macario, A. Aloise, G. Giordano, Catal. Today 175 (2011) 435–441.
[13] W. Chen, Z. Luo, C. Yu, G. Li, Y. Yang, J. Zhang, K. Lu, Fuel 135 (2014) 55–62.
[14] W. Chen, Z. Luo, C. Yu, Y. Yang, G. Li, J. Zhang, Fuel Process. Technol. 126 (2014) 420–428.
[15] Z. Tian, Q. Deng, L. Li, Adv. Mater. Res. 233–235 (2011) 1714–1717.
[16] Y. Kuwahara, T. Fujitani, H. Yamashita, Catal. Today 237 (2014) 18–28.
[17] V. Degirmenci, D. Uner, B. Cinlar, B.H. Shanks, A. Yilmaz, R.A. van Santen, E.J.M. Hensen, Catal. Lett. 141 (2011) 33–42.
[18] S. Perathoner, P. Lanzafame, G. Centi, F.C. Jentoft, T.V. Venkov, R. Schlögl, Stud. Surf. Sci. Catal. 170B (2007) 1788–1795.
[19] M. Imperor-Clerc, P. Davidson, A. Davidson, J. Am. Chem. Soc. 122 (2000) 11925–11933.
[20] B. Katryniok, S. Paul, M. Capron, S. Royer, C. Lancelot, L. Jalowiecki-Duhamel, V. Bellièr-Baca, P. Rey, F. Dumeignil, J. Mater. Chem. 21 (2011) 8159–8168.
[21] K. Amakawa, L. Sun, C. Guo, M. Haevecker, P. Kube, I.E. Wachs, S. Lwin, A.I. Frenkel, A. Patlolla, K. Hermann, R. Schlögl, A. Trunschke, Angew. Chem., Int. Ed. 52 (2013) 13553–13557.
[22] M.A. Ballem, J.M. Cordoba, M. Oden, J. Nanoparticle Res. 13 (2011) 2743–2748.
[23] Y. Wang, K.Y. Lee, S. Choi, J. Liu, L.Q. Wang, C.H.F. Peden, Green Chem. 9 (2007) 540–544.
[24] L.J. Gao, Q.Q. Shang, J.J. Zhou, G.M. Xiao, R.P. Wei, Asian J. Chem. 25 (2013) 6579–6583.
[25] S. Perathoner, P. Lanzafame, R. Passalacqua, G. Centi, R. Schlögl, D.S. Su, Micropor. Mesopor. Mater. 90 (2006) 347–361.
[26] R. Palkovits, C.M. Yang, S. Olejnik, F. Schüth, J. Catal. 243 (2006) 93–98.
[27] Sujandi, E.A. Prasetyanto, S.E. Park, Appl. Catal. A: Gen. 350 (2008) 244–251.
[28] X. Ji, K.T. Lee, M. Monjauze, L.F. Nazar, Chem. Commun. 36 (2008) 4288–4290.
[29] F.X. Zhang, X. Carrier, J.M. Krafft, Y.J. Yoshimura, J. Blanchard, New J. Chem. 34 (2010) 508–516.
[30] M.V. Landau, L. Vradman, X. Wang, L. Titelman, Micropor. Mesopor. Mater. 78 (2005) 117–129.
[31] A.H. Janssen, C.M. Yang, Y. Wang, F. Schüth, A.J. Koster, K.P. De Jong, J. Phys. Chem. B 107 (2003) 10552–10556.
[32] R.J. van Putten, J.C. van der Waal, E. de Jong, C.B. Rasrendra, H.J. Heeres, J.G. de Vries, Chem. Rev. 113 (2013) 1499–1597.
[33] O.O. James, S. Maity, L.A. Usman, K.O. Ajanaku, O.O. Ajani, T.O. Siyanbola, S. Sahu, R. Chaubey, Energy Environ. Sci. 3 (2010) 1833–1850.

[34] P. Lanzafame, S. Perathoner, G. Centi, F. Frusteri, J. Por. Mater 14 (2007) 305–313.
[35] S. Garg, K. Soni, G.M. Kumaran, R. Bal, K. Gora-Marek, J.K. Gupta, L.D. Sharma, G.M. Dhar, Catal. Today 141 (2009) 125–129.
[36] D. Tichit, B. Coq, H. Armendariz, F. Figuéras, Catal. Lett. 38 (1996) 109–113.
[37] A. Gulino, Anal. Bioanal. Chem. 405 (2013) 1479–1495.
[38] D. Briggs, J.T. Grant, Surface Analysis by Auger and X-Ray Photoelectron Spectroscopy, IMP, Chichester, UK, 2003.
[39] C. Perego, S. Peratello, Catal. Today 52 (1999) 133–145.
[40] D.Y. Zhao, Q.S. Huo, J.L. Feng, B.F. Chmelka, G.D. Stucky, J. Am. Chem. Soc. 120 (1998) 6024–6036.
[41] J. Sauer, F. Marlow, F. Schüth, Phys. Chem. Chem. Phys. 3 (2001) 5579–5584.
[42] X. Shi, Y. Wu, P. Li, H. Yi, M. Yang, G. Wang, Carbohyd. Res. 346 (2011) 480–487.
[43] A.S. Dias, M. Pillinger, A.A. Valente, J. Catal. 209 (2005) 414–423.
[44] C.K. Krishnan, T. Hayashi, M. Ogura, Adv. Mater. 20 (2008) 2131–2136.
[45] X. Liu, L. Sun, F. Lu, T. Li, X. Liu, J. Mater. Chem. A 1 (2013) 1623–1631.
[46] A.K. Mahmoud, Z. Fadhill, S.I. Al-nassar, F.I. Husein, E. Akman, A. Demir, J. Mater. Sci. Eng. B 3 (2013) 364–368.
[47] Y.T.E. Zong, H. Wan, Z. Xu, S. Zheng, D. Zhu, Micropor. Mesopor. Mater. 155 (2012) 192–200.
[48] M. Thommes, Chem. Ing. Technol. 82 (2010) 1056–1073.
[49] L. Vradman, M.V. Landau, D. Kantorovich, Y. Koltypin, A. Gedanken, Micropor. Mesopor. Mater. 79 (2005) 307–318.
[50] D.J. Zalewski, S. Alerasool, P.K. Doolin, Catal. Today 53 (1999) 419–432.
[51] B.M. Reddy, P.M. Sreekanth, P. Lakshmanan, J. Mol. Catal. A: Chem. 237 (2005) 93–100.
[52] A. Gulino, G.G. Condorelli, P. Mineo, I. Fragalà, Nanotechnology 16 (2005) 2170–2175.
[53] A. Gulino, R.G. Egdell, I. Fragalà, J. Mater. Chem. 11 (1996) 1805–1809.
[54] A. Gulino, S. La Delfa, I. Fragalà, R.G. Egdell, Chem. Mater. 8 (1996) 1287–1291.
[55] A. Gulino, G. Compagnini, R.G. Egdell, I. Fragalà, Thin Solid Films 352 (1999) 73–76.
[56] A. Gulino, R.G. Egdell, I. Fragalà, J. Am. Ceram. Soc. 81 (1998) 757–759.
[57] A. Gulino, R.G. Egdell, G. Baratta, G. Compagnini, I. Fragalà, J. Mater. Chem. 7 (1997) 1023–1027.
[58] F. Lønstad Bleken, K. Barbera, F. Bonino, U. Olsbye, K.P. Lillerud, S. Bordiga, P. Beato, T.V.W. Janssens, S. Svelle, J. Catal. 307 (2013) 62–73.
[59] K. Hadjiivanov, V. Avreyska, D. Klissurski, T. Marinova, Langmuir 18 (2002) 1619–1625.
[60] K. Hadjiivanov, J.C. Lavalley, Catal. Commun. 2 (2001) 129–133.
[61] E. Escalona Platero, M. Peñarroya Mentruit, C. Otero Areán, A. Zecchina, J. Catal. 162 (1996) 268–276.
[62] R. Buzzoni, S. Bordiga, G. Ricchiardi, C. Lamberti, A. Zecchina, G. Bellussi, Langmuir 12 (1996) 930–940.
[63] F. Bonino, A. Damin, S. Bordiga, C. Lamberti, A. Zecchina, Langmuir 19 (2003) 2155–2161.
[64] K. Barbera, F. Bonino, S. Bordiga, T.V.W. Janssens, P. Beato, J. Catal. 280 (2011) 196–205.
[65] C.A. Emeis, J. Catal. 141 (1993) 347–354.
[66] M. Hino, M. Kurashige, H. Matsuhashi, K. Arata, Thermochim. Acta 441 (2006) 35–41.
[67] A. Sinhamahapatra, N. Sutradhar, M. Ghosh, H.C. Bajaj, A.B. Panda, Appl. Catal. A: Gen. 402 (2011) 87–93.
[68] V. Bolis, G. Magnacca, G. Cerrato, C. Morterra, Top. Catal. 19 (2002) 259–269.
[69] K. Tanabe, H. Hattori, T. Yamaguchi, Crit. Rev. Surf. Chem. 1 (1990) 1–25.
[70] D.A. Ward, E.I. Ko, J. Catal. 150 (1994) 18–33.
[71] F.R. Chen, G. Coudurier, J.F. Joly, J.C. Vedrine, J. Catal. 143 (1993) 616–626.
[72] T. Riemer, D. Spielbauer, M. Hunger, G.A.H. Mekhemer, H. Knozinger, J. Chem. Soc., Chem. Commun. 10 (1994) 1181–1182.
[73] A. Clearfield, G.P.D. Serrette, A.H. Khazi-Syed, Catal. Today 20 (1994) 295–312.
[74] M.F. Gomez, L.A. Arrúa, M.C. Abello, React. Kinet. Catal. Lett. 73 (2001) 143–149.
[75] J. Horvat, B. Klaić, B. Metelko, V. Šunjić, Tetrahedron Lett. 26 (1985) 2111–2114.
[76] P. Che, F. Lu, J. Zhang, Y. Huang, X. Nie, J. Gao, Bioresour. Technol. 119 (2012) 433–436.